[12]The angular dependence was assumed to be $\exp(-3.9P\theta)$, where P is the K_L^0 momentum in GeV/c, and θ is the production angle, as given by G. Trilling, Lawrence Radiation Laboratory Report No. UCRL-16830 (unpublished), Vol. 1, p. 38.
[13]B. Rossi, *High Energy Physics* (Prentice-Hall, Englewood Cliffs, New Jersey, 1952), p. 32.
[14]This definition is in accord with J. Marx *et al.*, Ref. 5.
[15]M. N. Kreisler, Ph.D. dissertation, Stanford University, 1966 (unpublished), p. 83.
[16]B. Rossi, Ref. 13, p. 16.
[17]See, for example, G. Giacomelli, P. Pini, and S. Stagni, CERN Report No. CERN/HERA 69-1., 1969 (unpublished).
[18]O. I. Dahl *et al.*, Phys. Rev. 163, 1430 (1967).
[19]J. D. Jackson and R. L. McCarthy, Phys. Rev. B 6, 4131 (1972).
[20]A. R. Clark *et al.*, Phys. Letters 41B, 229 (1972).
[21]A. O. Weissenberg, *Muons* (North-Holland, Amsterdam, 1967), p. 15.
[22]A. O. Weissenberg, Ref. 21, p. 177.
[23]A. O. Weissenberg, Ref. 21, p. 163.
[24]C. S. Johnson *et al.*, Phys. Rev. 125, 2111 (1962).
[25]D. Quitmann *et al.*, Nucl. Phys. 51, 609 (1964).
[26]B. Rossi, Ref. 13, p. 78.
[27]A. O. Weissenberg, Ref. 21, p. 175.

PHYSICAL REVIEW D VOLUME 7, NUMBER 3 1 FEBRUARY 1973

Production of K_L^0 Mesons and Neutrons from Electrons on Beryllium Above 10 GeV*

G. W. Brandenburg, A. D. Brody, W. B. Johnson, D. W. G. S. Leith, J. S. Loos,† G. J. Luste,‡ J. A. J. Matthews, K. Moriyasu,§ B. C. Shen,‖ W. M. Smart,** F. C. Winkelmann, and R. J. Yamartino
Stanford Linear Accelerator Center, Stanford University, Stanford, California 94305
(Received 14 August 1972)

Measurements are presented of the yields of K_L^0 mesons and neutrons produced by electrons of energies between 10 and 19 GeV incident on 0.70- and 1.75-radiation-length beryllium targets for production angles between 1.6° and 4°. Values for the K_L^0 absorption cross section on lead are also found for momenta between 1.4 and 7.4 GeV/c. A successful interpretation of K_L^0 production is made in terms of the process $\gamma N \to K_L^0 X$, where X represents an inclusive sum over all final states. The invariant structure function for K_L^0 photoproduction, extracted from the Be yields, is found to be simply related to the result for hydrogen by an over-all multiplicative factor, A_{eff}, the effective number of nucleons in the target nucleus. The results of the theoretical analysis are also compared to charged-K photoproduction and extrapolated to electron energies of 50 GeV.

I. INTRODUCTION

We present measurements of the yield of K_L^0 mesons and neutrons produced from electrons incident on a beryllium target at energies between 10 and 19 GeV. Table I summarizes the specific electron energies, production angles, and Be target thicknesses for which these measurements have been made. The data were acquired during three separate data runs at the Stanford Linear Accelerator Center (SLAC) in which the SLAC 40-in. hydrogen-filled bubble chamber was exposed to a neutral beam. A description of the neutral beam is given in Sec. II. A preliminary report of the results for run I is given in Ref. 1. Measurements of K_L^0 photoproduction below 10 GeV on complex nuclei have also been made in other experiments.[2-5]

The yields of K_L^0 and neutrons are presented in Secs. III and IV, respectively. The yields are found to behave similarly above ~4 GeV/c, where both show a rapid falloff with increasing momentum of the neutral particle. However, for momenta below ~2 GeV/c the neutron yield has an intense low-energy component which is not present in the K_L^0 yield. This low-energy component is probably due to the disintegration of the target nucleus.

The present measurements of K_L^0 yields, together with previous measurements,[1-3] suggest that the photoproduction of K^0 mesons is a complicated process with contributions not only from the obvious two-body and quasi-two-body reactions but also from multiparticle channels. A natural framework for dealing with such a complicated situation is provided by the inclusive single-particle production process, $\gamma N \to K_L^0 X$, where X represents the sum of all final-state configurations. In Sec. V, we discuss the K_L^0 yields in terms of inclusive K_L^0 production and find a satisfactory description for the measurements. Extrapolations are then made for K_L^0 yields at higher energies and for various target thicknesses. Comparisons are also made to the available yield data for K^+ and K^- mesons.

TABLE I. Target thicknesses, electron energies, and production angles for K_L^0 and n yields in the present experiment.

Experimental run	Thickness of Be target (r.l.)	e^- energy (GeV)	Production angle	Particle yields reported
I	1.75	10	2°	K_L^0
			4°	K_L^0
		16	2°	K_L^0 and n
			3°	K_L^0 and n
			4°	K_L^0 and n
II	0.70	16	1.6°	K_L^0
		18	1.6°	K_L^0
III	1.75	19	1.6°	K_L^0 and n

II. NEUTRAL SECONDARY BEAM

A schematic illustration of the neutral beam is shown in Fig. 1. The primary electron beam first passed through a toroid charge monitor[6] which integrated the total charge per pulse for purposes of beam normalization. The production angle of the neutral beam with respect to the electron beam could be varied from 1.5° to 5° by a dipole magnet placed immediately upstream of the Be target. The position, spot size, and angle of entry of the electron beam on the target was monitored visually by means of closed-circuit television displays of two ruled zinc sulfide screens. The first screen was attached to the upstream face of the target and the second was attached to the upstream face of a water-cooled dump used to stop the electron beam. The neutral beam channel was defined by three carefully aligned lead collimators: a 2.2-m tapered collimator centered 7 m from the target and two 0.5-m untapered collimators located 10 m and 22 m from the target. Two sweeping magnets were used to remove charged particles. The halo of muons was absorbed by ~15 m of iron shielding surrounding the neutral beam channel. The photons in the beam were absorbed by placing suitable amounts of material in the beam, as summarized in Table II. At the bubble chamber (55 m from the target) the beam had a cross-sectional area of 15 cm by 40 cm and subtended a solid angle of ~2 $\times 10^{-5}$ sr.

III. K_L^0 YIELDS

A. Selection of Events

The film was scanned for the visible K_L^0 decays $K_L^0 \to \pi^\pm e^\mp \nu$, $K_L^0 \to \pi^\pm \mu^\mp \nu$, and $K_L^0 \to \pi^+\pi^-\pi^0$. These decays appear mainly as two-prong events which are not associated with any interaction in the chamber. However, a small fraction of the final sample of events (8%) were first classified by the scanners as associated with an interaction in the chamber, but were properly reclassified as beam decays following measurement. The decay tracks were measured either on the SLAC spiral reader or on film-plane digitizers and spatially reconstructed with the program TVGP. The reconstructed tracks and the K_L^0 direction were then used to obtain kinematic solutions to the above decay modes. Events were included in the analysis of the K_L^0 momentum spectrum if any of the five decay modes were kinematically possible.[7] Events were excluded if any of the following were satisfied:

$$M(e^+e^-) < 35 \text{ MeV},$$

$$485 < M(\pi^+\pi^-) < 510 \text{ MeV},$$

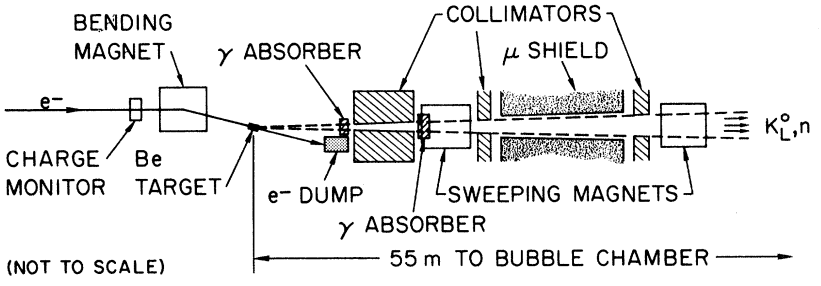

FIG. 1. Schematic illustration of the neutral secondary beam.

TABLE II. Photon absorbers used in secondary neutral beams.

e^- energy (GeV)	Production angle	Amount of material in secondary beam (g/cm^2) Hydrogen [a]	Lithium [a]	Tungsten	Lead
10	2°	6.5	44.6	147.1	173.0
10	4°	6.5	44.6	147.1	173.0
16	2°	6.5	44.6	147.1	173.0
16	3°	6.5	44.6	147.1	173.0
16	4°	6.5	44.6	147.1	173.0
16	1.6°	9.7	65.0	98.0	216.2
18	1.6°	9.7	65.0	98.0	259.5
19	1.6°	3.3	22.3	98.0	230.6

[a] The hydrogen and lithium were in the form of compressed blocks of lithium hydride powder kept in an inert atmosphere.

or

$$1110 < M(p\pi^-) < 1120 \text{ MeV},$$

where the charged tracks were interpreted as the indicated particles. These cuts, which effectively remove all non-K_L^0 decays, also remove a small fraction (~5%) of the K_L^0 decays. However, these cuts introduce no bias since the same cuts are made on the Monte Carlo events used in the theoretical analysis (see below). A final selection required the K_L^0 decay to occur within a 55-cm-long decay volume within the chamber.

B. Determination of the K_L^0 Momentum Spectrum at the Bubble Chamber

The method of analysis described below determines both the shape and the absolute magnitude of the K_L^0 momentum spectrum at the bubble chamber from the observed distribution of the visible momentum, p_{vis}, defined as

$$p_{vis} = \hat{n} \cdot (\vec{p}_1 + \vec{p}_2),$$

where $\vec{p}_1$ and $\vec{p}_2$ are the three-momenta of the two charged tracks, and $\hat{n}$ is a unit vector along the beam direction. On the average, the quantity p_{vis} is roughly $\frac{2}{3}$ of the K_L^0 momentum, p_K, regardless of decay mode; therefore, the p_{vis} distribution depends sensitively on the shape of the p_K distribution. The absolute intensity of the K_L^0 flux is fixed by the known K_L^0 lifetime and the branching ratio $(K_L^0 \to \text{charged})/(K_L^0 \to \text{all})$.[8]

In Fig. 2, we illustrate the procedure used to determine the momentum distribution of the K_L^0 particles which decay in the chamber. First the p_{vis} data are binned such that for the ith bin there are N_i events between $p_{vis\,i}$ and $p_{vis\,i} + \Delta p_{vis\,i}$. The momentum distribution of decays, denoted $Z(p_K)$, is then represented by a histogram, the jth bin of which covers the interval from p_{Kj} to $p_{Kj} + \Delta p_{Kj}$. The height of the jth bin, $Z(p_{Kj})$, is denoted by the parameter α_j. For each bin in p_K a p_{vis} distribution is then generated by Monte Carlo techniques[9]; for the jth bin in p_K the p_{vis} distribution normalized to unity is denoted H_{ji}, where the in-

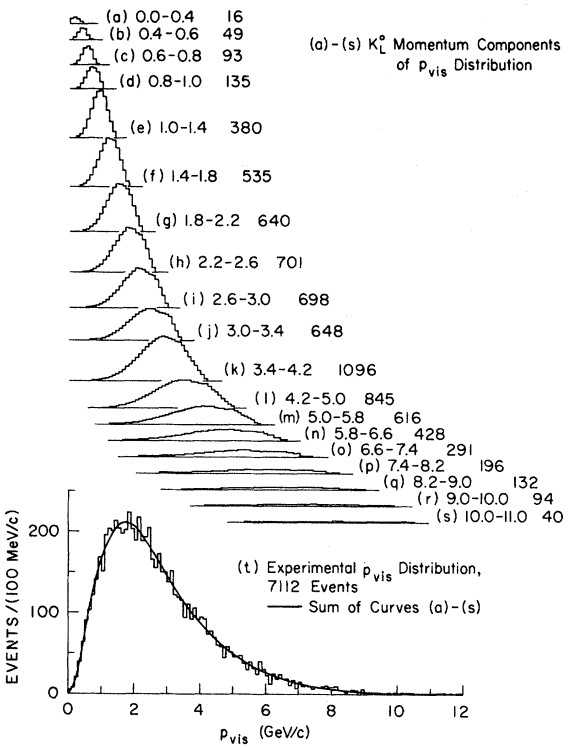

FIG. 2. Distribution in p_{vis} used to determine the K_L^0 momentum spectrum from 16-GeV electrons incident at 2° production angle on a 1.75-r.l. Be target. The variable p_{vis} is the visible momentum from the three-body K_L^0 decays, as explained in the text. (a)–(s) Monte Carlo-generated component histograms corresponding to the indicated narrow K_L^0 momentum intervals. The intensities of the histograms are determined by a fit to the p_{vis} spectrum. (*t*) Experimental p_{vis} spectrum. The solid curve is the summation of the fitted component histograms.

dex i runs over all p_{vis} bins. Each p_{vis} distribution is comprised of events from the five main K_L^0 charged decay modes generated according to the standard decay matrix elements in proportion to their known decay rates.[8] The mass cuts used for the data selection (see Sec. III A) are also applied to the Monte Carlo events. For an assumed set of α_j values, the expected number of events in the ith p_{vis} bin is then given by

$$T_i = \sum_j \alpha_j H_{ji} .$$

The best set of values for the α_j's is then determined by minimizing $\chi^2(\alpha_1, \alpha_2, \ldots)$, where

$$\chi^2(\alpha_1, \alpha_2, \ldots) \equiv \sum_i (T_i - N_i)^2 / T_i .$$

The value of α_j at the minimum of χ^2, α_j^*, is equal to $Z(p_{Kj})$.[10] In order to determine the statistical uncertainties in α_j^*, a number of successive re-minimizations of χ^2 (typically 50) are done after independently changing each p_{vis} bin from its original value, T_i, to $T_i \pm \delta T_i$, where δT_i is randomly chosen on successive minimizations according to a Gaussian distribution having a standard deviation equal to $T_i^{1/2}$. The standard deviations of the values of α_j^* thus obtained are taken to be the statistical uncertainties.

The procedure outlined above is illustrated in Fig. 2 for a K_L^0 beam produced at 2° by 16-GeV electrons on a 1.75-radiation-length (r.l.) Be target. The p_{vis} distributions corresponding to the fitted components of the $Z(p_K)$ distribution are summed to provide the solid curve on the experimental p_{vis} distribution. This curve is seen to reproduce the p_{vis} spectrum very well.

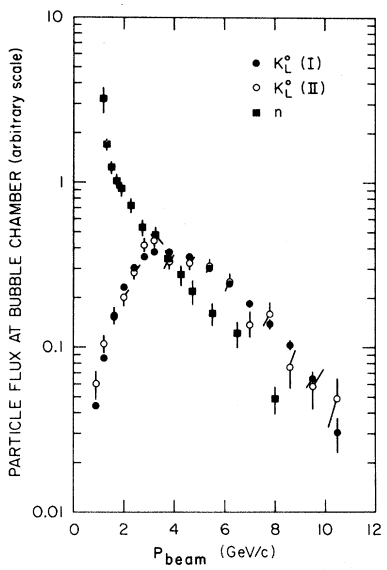

FIG. 3. Comparison of the K_L^0 flux (○,●) and neutron flux (■) at the hydrogen bubble chamber. This comparison is a typical example of the relative K_L^0/n fluxes at the experimental apparatus, but this ratio does depend on the amount of photon absorber in the beam, the production angle, and the distance between the target and apparatus. The solid and open circles result from different methods of analysis of the K_L^0 spectrum (see text).

The absolute flux of K_L^0 at the chamber, denoted by $F(p_K)$, is related to $Z(p_K)$ as follows:

$$F(p_K) = \frac{1}{\epsilon r}(1 - e^{-L/\lambda(p_K)})^{-1} Z(p_K) ,$$

where

ϵ = efficiency factor for scanning and measuring of the film,

r = branching ratio, $(K_L^0 \to \text{charged})/(K_L^0 \to \text{all})$,

$\lambda(p_K) = p_K c\tau / m_K$, the mean K_L^0 decay length,

L = length of decay volume in the chamber,

$m_K = K_L^0$ mass,

and

$\tau = K_L^0$ lifetime.

An example of the K_L^0 flux at the chamber is shown in Fig. 3. The uncertainties shown are the statistical uncertainties determined as described above.

As a check of the preceding method we have also determined the K_L^0 spectrum at the chamber by an alternate method.[11] First, by means of a transverse-momentum selection, a sample of unique K_{e3} decays is isolated. This selection retains approximately 15% of the total number of K_L^0 decays. Each of these decays has up to four kinematical solutions for p_K, and each of the solutions is assigned a weight which is normalized such that the total weight for a single decay is unity. The individual weights are proportional to a product of the Dalitz-plot density, the Jacobian relating p_K to the measured variables, and the K_L^0 spectrum. Thus the spectrum is given by

$$Z(p_{Kj}) = \sum_{i=1}^{N_j} W_{ij}(Z) ,$$

where the $W_{ij}(Z)$ are the weights of the N_j kinematical solutions in the jth p_K bin. Since the weights are functions of the K_L^0 spectrum (Z), this expression is a set of m nonlinear equations, where m is the number of p_K bins. These can be solved iteratively by substituting the spectrum Z of the previous iteration into $W_{ij}(Z)$ to obtain a new solution. Using an arbitrary spectrum as a starting value, this procedure converges after a few iterations to a unique solution for $Z(p_K)$. The open circles in Fig. 3 show a K_L^0 spectrum obtained by this meth-

od, where $Z(p_K)$ has been converted to flux at the chamber. The agreement with the previously described spectrum determination is excellent, although the error bars are larger due to the smaller statistics.

C. Determination of K_L^0 Yields at the Target from K_L^0 Fluxes at the Chamber

If $F(p_K)$ is the flux of K_L^0 mesons per GeV/c at the chamber, D the distance between target and chamber, $\Delta\Omega$ the solid angle of the detector, and N_e the number of electrons incident on the target, then the yield is given by

$$Y_K(p_K) = F(p_K)\exp[D/\lambda(p_K)] \times \exp\left[\sum_i a_i \sigma_{Ki}(p_K)\right] \Big/ (N_e \Delta\Omega),$$

expressed in units of K_L^0/electron sr (GeV/c). The first exponential factor corrects for the loss of K_L^0 particles due to decays in flight. The second exponential factor corrects for absorption of the K_L^0 beam in the photon absorbers (see Table II), where, for the ith absorber, $\sigma_{Ki}(p_K)$ is the total K_L^0 absorption cross section for momentum p_K, $a_i = \rho_i N_0/A_i$, ρ_i is the amount of absorber in g/cm^2, A_i is the atomic weight, and N_0 is Avogadro's number.

The solid-angle factor, $\Delta\Omega$, has been determined from the geometry of the neutral beam; corrections for collimator edges have been made by a study of the distribution of K_L^0 decay positions within the bubble chamber. The number of incident electrons, N_e, has been measured for each accelerator pulse in the toroid charge monitor and summed over the pulses for each yield curve.

Values for the absorption cross sections for Li, W, and Pb have been interpolated from the K_L^0-nucleus measurements of Lakin *et al.*[12] and the $K^\pm$-nucleus measurements of Abrams *et al.*[13] In addition, values for the K_L^0-Pb absorption cross section have been measured in the present experiment and are presented in Table III.[14] The available K-nucleus cross sections are shown in Fig. 4 together with interpolation curves which, for atomic weight A and momentum p_K, are given by the empirical parametrization[15]

$$\sigma(p_K, A) = [b_1(p_K + b_2 A)^{-n_1} + b_3]A^{n_2}. \quad (1)$$

Values for the $K_L^0 p$ absorption cross section have been interpolated from $K^\pm n$ measurements,[16-18] also shown in Fig. 4, where the interpolation curve is of the form[15]

$$\sigma(p_K) = b_4 p_K^{-n_3} + b_5.$$

The K_L^0-yield results for the 1.75-r.l. Be target are presented in Table IV and Fig. 5; the results for the 0.70-r.l. Be target are presented in Table V and Fig. 6. The quoted uncertainties are the statistical uncertainties in $F(p_K)$ discussed in Sec. III B. All the yield curves have a broad maximum for p_K equal to ~15% of the incident electron energy. The falloff in yield at larger p_K values becomes more rapid as the target thickness is increased and as the production angle is increased. The curves shown on Figs. 5 and 6 are discussed in detail in Sec. V.

TABLE III. K_L^0-Pb absorption cross sections.

K_L^0 momentum (GeV/c)	σ [a] (mb)
1.4–2.6	2730 ± 100
2.6–3.4	2660 ± 120
3.4–5.0	2540 ± 130
5.0–7.4	2370 ± 140

[a] The uncertainties quoted are statistical only. The over-all systematic error is estimated to be ±5%.

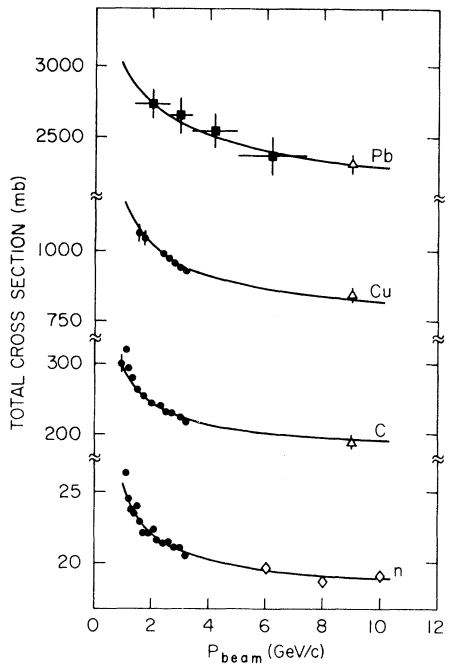

FIG. 4. Absorption cross sections for K mesons on various absorbers. The data are from the following sources: (■) K_L^0-Pb (this experiment); (△) K_L^0-Pb, K_L^0-Cu, and K_L^0-C (Ref. 12); (●) average of K^+ and K^- on Cu, C, and n (Refs. 13, 16, 17); (◇) average of K^+ and K^- on n (Ref. 18). The curves shown are empirical interpolations described in the text.

TABLE IV. K_L^0 yields for electrons incident on 1.75-r.l. Be target.

Electron energy (GeV)	10	10	16	16	16	19
Production angle	2°	4°	2°	3°	4°	1.6°
No. events in p_{vis} distribution	821	601	7112	2149	1524	2468
K_L^0 momentum interval (GeV/c)	Yield at target [K_L^0/(10^4 electrons) sr (GeV/c)]					
1.0–1.5	1.10 ± 0.13	1.12 ± 0.13	2.40 ± 0.12	1.92 ± 0.15	1.70 ± 0.20	2.40 ± 0.20
1.5–2.0	1.18 ± 0.10	1.19 ± 0.11	2.59 ± 0.12	2.10 ± 0.13	1.89 ± 0.17	2.76 ± 0.15
2.0–2.5	1.21 ± 0.10	1.12 ± 0.10	2.70 ± 0.12	2.15 ± 0.13	2.00 ± 0.16	3.00 ± 0.15
2.5–3.0	1.19 ± 0.10	0.93 ± 0.09	2.62 ± 0.11	2.06 ± 0.12	1.99 ± 0.14	3.17 ± 0.15
3.0–3.5	1.08 ± 0.11	0.65 ± 0.09	2.44 ± 0.11	1.89 ± 0.12	1.78 ± 0.12	3.13 ± 0.15
3.5–4.0	0.86 ± 0.13	0.42 ± 0.08	2.14 ± 0.10	1.67 ± 0.11	1.53 ± 0.10	2.94 ± 0.15
4.0–4.5	0.61 ± 0.11	0.27 ± 0.07	1.85 ± 0.10	1.46 ± 0.10	1.24 ± 0.09	2.70 ± 0.14
4.5–5.0	0.38 ± 0.10	0.18 ± 0.06	1.58 ± 0.10	1.25 ± 0.09	1.01 ± 0.08	2.45 ± 0.14
5.0–6.0	0.16 ± 0.06	0.12 ± 0.05	1.21 ± 0.09	0.96 ± 0.08	0.74 ± 0.07	2.10 ± 0.12
6.0–7.0	0.06 ± 0.03		0.84 ± 0.07	0.62 ± 0.07	0.48 ± 0.06	1.66 ± 0.11
7.0–8.0			0.54 ± 0.05	0.38 ± 0.05	0.32 ± 0.05	1.34 ± 0.10
8.0–9.0			0.35 ± 0.04	0.23 ± 0.04	0.19 ± 0.05	1.04 ± 0.09
9.0–10.0			0.21 ± 0.03	0.14 ± 0.04	0.01 ± 0.04	0.76 ± 0.08
10.0–11.0			0.09 ± 0.03	0.07 ± 0.03		0.50 ± 0.07
11.0–12.0			0.05 ± 0.02			0.31 ± 0.06
12.0–13.0						0.17 ± 0.06

D. Estimates of Systematic Uncertainties in the K_L^0 Yields

The relative systematic uncertainties between the various K_L^0 yields are estimated to be 15%, with the following contributions taken in quadrature: film analysis (5%), solid angle (5%), and targeting (focus and intensity) of the electron beam (10%).

The over-all systematic uncertainty in the scale of the K_L^0 yields is estimated to be 20%, and is comprised of ~15% uncertainty in the absorption factor and ~10% uncertainty in the film analysis.

TABLE V. K_L^0 yields for electrons incident on 0.70-r.l. Be target.

Electron energy (GeV)	16	18
Production angle	1.6°	1.6°
No. events in p_{vis} distribution	4195	2117
K_L^0 momentum interval (GeV/c)	Yield at target [K_L^0/(10^4 electrons) sr (GeV/c)]	
1.0–1.5	0.83 ± 0.09	0.92 ± 0.09
1.5–2.0	1.00 ± 0.08	1.09 ± 0.09
2.0–2.5	1.13 ± 0.08	1.21 ± 0.09
2.5–3.0	1.17 ± 0.07	1.27 ± 0.08
3.0–3.5	1.14 ± 0.07	1.24 ± 0.08
3.5–4.0	1.10 ± 0.07	1.20 ± 0.08
4.0–4.5	1.03 ± 0.07	1.11 ± 0.07
4.5–5.0	0.96 ± 0.07	1.04 ± 0.07
5.0–6.0	0.82 ± 0.07	0.89 ± 0.07
6.0–7.0	0.60 ± 0.06	0.68 ± 0.06
7.0–8.0	0.40 ± 0.05	0.50 ± 0.06
8.0–9.0	0.25 ± 0.04	0.36 ± 0.05
9.0–10.0	0.13 ± 0.03	0.26 ± 0.04
10.0–11.0	0.06 ± 0.02	0.16 ± 0.04
11.0–12.0		0.09 ± 0.03

IV. NEUTRON YIELDS

A. Selection of Events

The neutron flux at the bubble chamber has been determined from a sample of events from the reaction

$$np \to pp\pi^-,$$

which appear as three-prong interactions in the chamber. The candidates have been measured on the SLAC spiral reader, and spatially reconstructed and kinematically fitted with the programs TVGP and SQUAW. These events have three kinematic constraints, since the direction of the beam and the momenta of all outgoing tracks are measured. For momenta above ~5 GeV/c, a fraction of the events (~10–15%) are kinematically ambiguous with the reaction $K^0p \to pK^+\pi^-$. However, the majority of the ambiguities are resolved on the basis of the χ^2 probabilities of the kinematic fits, and we estimate that the remaining contamination from the K^0p events is less than 5% at all momenta. The same samples of film and the same active volume in the chamber were used for the $np \to pp\pi^-$ events as for the K_L^0 decays.

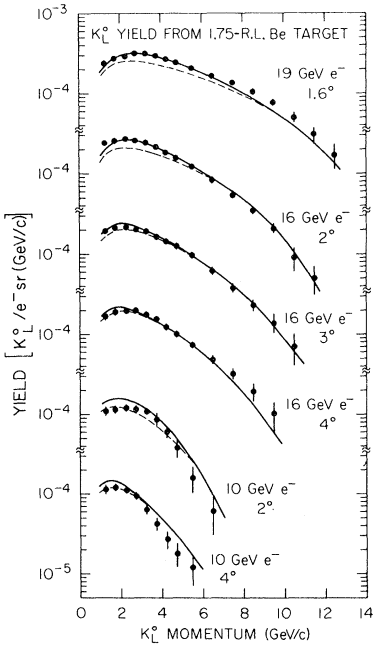

FIG. 5. Yields of K_L^0 mesons from electrons incident on a 1.75-r.l. Be target. The various electron energies and production angles are indicated. The curves represent an interpretation of the yields (discussed in detail in the text) in terms of the inclusive K_L^0 photoproduction from the individual nucleons in the Be nucleus together with the coherent ϕ (1020) photoproduction from the entire nucleus. The sum of these two processes is shown by the solid curves, whereas the inclusive production alone is shown by the dashed curves.

B. Determination of the Neutron Momentum Spectrum at the Bubble Chamber

For a given neutron momentum, p_n, the neutron flux at the chamber per GeV/c is given by

$$F(p_n) = C\,N(p_n)/\sigma(np \to pp\pi^-),$$

where $N(p_n)$ is the number of observed $np \to pp\pi^-$ events per GeV/c, and the constant of proportionality, C, is determined from the density of the liquid hydrogen and the length of the interaction region.

Values for $\sigma(np \to pp\pi^-)$ have been interpolated from the pd experiments of Batson *et al.*,[19] Cohn *et al.*,[20] Brunt *et al.*,[21] Shapira *et al.*,[22] and Rushbrooke *et al.*[23] and from the np experiment of Gasparyan *et al.*[24] These cross-section data are plotted in Fig. 7 together with a hand-drawn interpolation curve (the solid curve) used for the present analysis. The dashed curves represent our estimate of the uncertainty of the interpolation curve.

An example of the neutron flux at the chamber is shown in Fig. 3 for comparison to the K_L^0 flux. The uncertainties shown are dominated by the uncertainty in $\sigma(np \to pp\pi^-)$ rather than the statistical error on $N(p_n)$. The neutron flux peaks below 1 GeV/c, and the n/K_L^0 ratio is seen to decrease by an order of magnitude over the range from 2 to 6 GeV/c. For this example the flux of neutrons becomes equal to the flux of K_L^0 mesons for $p \sim 3$ GeV/c. However, the n/K_L^0 ratio at the chamber depends on the amount of absorber in the neutral beam and is diminished as the amount of absorber is increased since the nuclear absorption cross

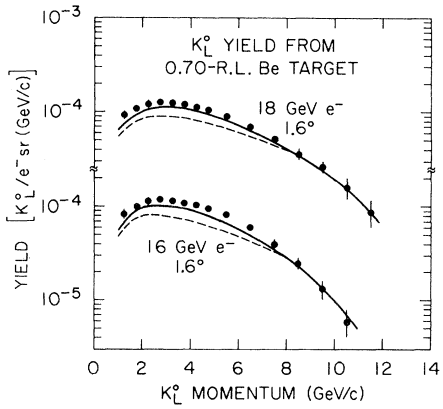

FIG. 6. Yields of K_L^0 mesons from electrons incident on 0.70-r.l. Be target. The electron energies and production angles are indicated. The meaning of the curves is discussed in the caption to Fig. 5.

sections are larger for neutrons than for K_L^0 mesons.

C. Determinations of Neutron Yields at the Target from Neutron Fluxes at the Chamber

If $F(p_n)$ is the number of neutrons per GeV/c at the chamber, $\Delta\Omega$ the solid angle of the detector, and N_e the number of electrons incident on the target, then the yield is given by

$$Y_n(p_n) = F(p_n) \exp\left[\sum_i a_i \sigma_{ni}(p_n)\right] \Big/ (N_e \Delta\Omega),$$

expressed in units of neutrons/electron sr (GeV/c). The same values for N_e, $\Delta\Omega$, and the a_i's apply to the neutron yields as applied to the K_L^0 yields (see Sec. III C).

Values for neutron absorption cross sections for Li, W, and Pb have been interpolated from the measurements of Refs. 12 and 25–30. Values for np total cross sections have been interpolated from the measurements of Refs. 31–33.

The results for the neutron yields are given in Table VI and Fig. 8. The quoted uncertainties are the sum in quadrature of the statistical uncertainty in $N(p_n)$ and the estimated uncertainty of the interpolation curve for $\sigma(p_n)$ shown in Fig. 7. The neutron yields have an intense low-energy component below ~2 GeV/c. Since this low-energy component is not present in the K_L^0 yields, it must arise from the disintegration of Be nuclei in the target. For momenta above ~4 GeV/c the yield of neutrons and K_L^0 mesons from the 1.75-r.l. Be target have similar dependences on momentum, with the ratio n/K_L^0 being in the range ~1.2 to ~1.7.

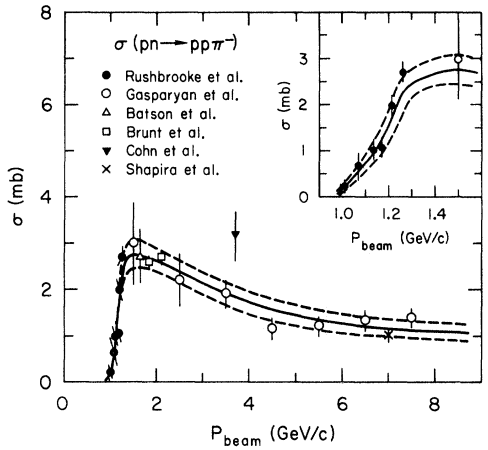

FIG. 7. Summary of cross-section values for the reaction $np \to pp\pi^-$. The inset shows the low-energy data on an expanded momentum scale. The data sources are (△) Ref. 19, (▼) Ref. 20, (□) Ref. 21, (×) Ref. 22, (●) Ref. 23, and (○) Ref. 24. The solid curve is a hand-drawn interpolation curve used to extract neutron flux at the chamber. The dashed curves represent our estimate of the uncertainty in the extrapolation curve.

D. Estimates of Systematic Uncertainties in the Neutron Yields

The relative systematic uncertainties between the various neutron yields is estimated to be 15%,

TABLE VI. Neutron yields for electrons incident on 1.75-r.l. Be target.

Electron energy (GeV)	16	16	16	19
Production angle	2°	3°	4°	1.6°
No. events $np \to pp\pi^-$	10596	3809	2722	3297
n momentum interval (GeV/c)	Yield at target [n/(10^4 electrons) sr (GeV/c)]			
1.1–1.2	12.27 ± 3.00	11.22 ± 2.87	10.85 ± 2.81	10.34 ± 2.71
1.2–1.4	9.99 ± 1.31	9.52 ± 1.30	9.04 ± 1.26	9.13 ± 1.28
1.4–1.6	9.74 ± 1.10	8.15 ± 0.98	8.54 ± 1.04	8.41 ± 1.03
1.6–1.8	9.03 ± 1.04	8.99 ± 1.09	7.35 ± 0.93	8.83 ± 1.10
1.8–2.0	8.68 ± 0.86	7.35 ± 0.81	6.98 ± 0.80	7.60 ± 0.86
2.0–2.5	7.31 ± 0.75	6.52 ± 0.70	5.46 ± 0.61	6.84 ± 0.75
2.5–3.0	5.77 ± 0.66	5.47 ± 0.66	5.24 ± 0.65	5.40 ± 0.67
3.0–3.5	5.20 ± 0.67	4.33 ± 0.60	4.04 ± 0.58	5.00 ± 0.70
3.5–4.0	3.88 ± 0.56	3.91 ± 0.59	3.12 ± 0.50	3.87 ± 0.60
4.0–4.5	3.14 ± 0.50	3.45 ± 0.58	2.30 ± 0.42	4.09 ± 0.69
4.5–5.0	2.49 ± 0.44	2.20 ± 0.42	2.00 ± 0.40	3.30 ± 0.62
5.0–6.0	1.80 ± 0.28	1.56 ± 0.27	1.35 ± 0.24	2.57 ± 0.42
6.0–7.0	1.34 ± 0.24	1.24 ± 0.24	0.86 ± 0.19	1.78 ± 0.34
7.0–9.0	0.52 ± 0.10	0.53 ± 0.12	0.32 ± 0.08	1.03 ± 0.21

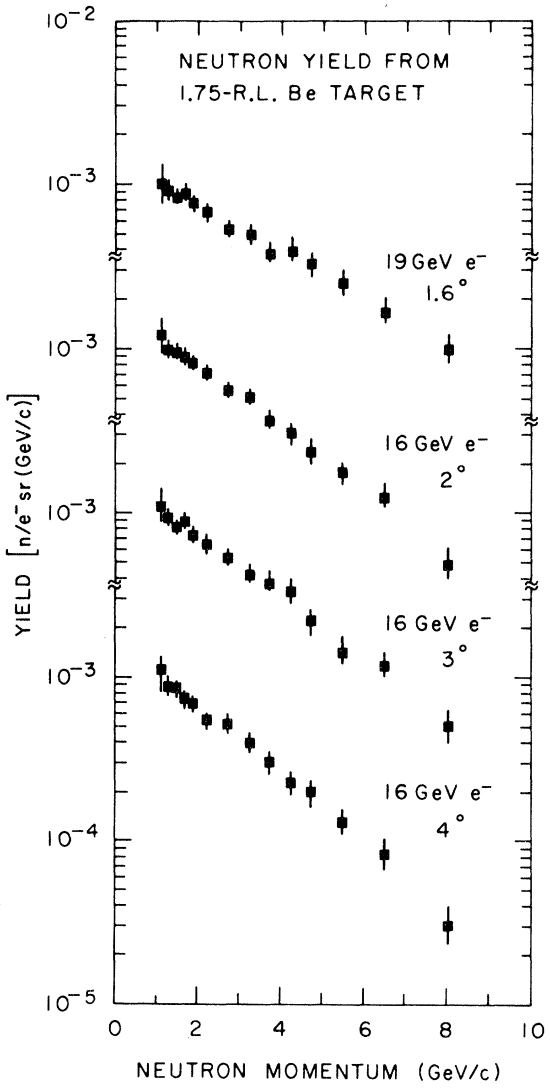

FIG. 8. Yields of neutrons from electrons incident on a 1.75-r.l. Be target. The electron energies and production angles are indicated.

the same as for the relative systematic uncertainty between the various K_L^0 yields (see Sec. III D).

The over-all systematic uncertainty in the scale of the neutron yields is estimated to be 20%, and is made up of ~15% uncertainty in the absorption factor and ~10% uncertainty in the film analysis.

V. INTERPRETATION OF K_L^0 YIELDS

A. Theoretical Analysis

The production of hadronic particles from high-energy electrons incident on thick targets can be described qualitatively by the following sequence of steps: (a) Real photons[34] are produced by bremsstrahlung throughout the volume of the target, (b) particles are photoproduced from the target nuclei, and (c) a fraction of the hadronic particles are absorbed before leaving the target. Although steps (a) and (c) are well understood and readily parametrized, step (b) is in general a complicated summation over many processes, and has not been systematically parametrized in previous studies.

The aim of this section is to obtain a simple description of the measured K_L^0 yields by considering only two production processes. The more important contribution is incoherent photoproduction from the individual nucleons in the target nucleus, $\gamma N \to K_L^0 X$, where X represents the inclusive sum over all final-state configurations. The second contribution is from the reaction $\gamma\mathrm{Be} \to \phi(1020)\mathrm{Be}$, $\phi(1020) \to K_L^0 K_S^0$, which we assume to be the only important coherent process for K_L^0 photoproduction.

The quantitative description for steps (a)–(c) for the yield of hadronic particles having laboratory momentum p (GeV/c) and laboratory production angle θ, from a target of thickness T [in units of radiation length (r.l.)], for electrons incident with energy E_0 (GeV), is given by the following relation[35]:

$$Y(p,\theta;T,E_0) = \left(\frac{N_0 X_0}{2\pi A}\right)\int_0^T dt \int_{k_{\min}}^{E_0} dk e^{-\eta(p)(T-t)} \times I_\gamma(k,E_0,t)\,\frac{d^2\sigma(k)}{dp d\cos\theta} \tag{2}$$

in units of particles/electron sr (GeV/c). In this expression k is the photon energy, $I_\gamma(k,E_0,t)$ is the distribution in energy of the photons for a single electron of energy E_0 incident on a target of thickness t, $d^2\sigma/dp d\cos\theta$ is the differential cross section for photoproduction of the hadronic particles, $k_{\min}$ is the minimum energy kinematically allowed, N_0 is Avagadro's number, X_0 is the unit r.l. of the target material in g/cm^2, and A is the atomic weight of the target nucleus. The factor $\eta(p)$ accounts for the absorption of the hadronic particles leaving the target and is given by

$$\eta(p) = \left(\frac{N_0 X_0}{A}\right)\sigma(p),$$

where $\sigma(p)$ is the absorption cross section for the target nucleus. For the beryllium nucleus we have used the empirical parametrization of Eq. (1) for $\sigma(p)$. The photon energy distribution is given by the thick-target approximation of Tsai and Whitis[35]:

$$I_\gamma(k,E_0,t) = \frac{1}{k}\,\frac{(1-k/E_0)^{(4/3)t} - e^{-(7/9)t}}{\frac{7}{9}+\frac{4}{3}\ln(1-k/E_0)}\,.$$

In order to describe K_L^0 yields by electrons on

thick targets, the single-particle differential cross section for K_L^0 photoproduction must be known. In the present analysis, we assume

$$\frac{d^2\sigma}{dpd\cos\theta} = \left(\frac{d^2\sigma}{dpd\cos\theta}\right)_{\text{incoherent}} + \left(\frac{d^2\sigma}{dpd\cos\theta}\right)_{\text{coherent}},$$

where the incoherent part is inclusive K_L^0 photoproduction from the individual nucleons and the coherent part is $\phi(1020)$ photoproduction from the entire target nucleus.

For each measured K_L^0 yield point, the value for $(d^2\sigma/dpd\cos\theta)_{\text{coherent}}$ is calculated by a Monte Carlo integration for the two-step process: $\gamma\text{Be} \rightarrow \phi(1020)\text{Be}$, $\phi(1020) \rightarrow K_L^0 K_S^0$. The differential cross section is interpolated from the measurements of McClellan *et al.*[36] of $\phi(1020)$ photoproduction from complex nuclei and is assumed to be independent of energy:

$$\frac{d\sigma}{dt}(\gamma\text{Be} \rightarrow \phi(1020)\text{Be}) = 125e^{40t}\ \mu\text{b/GeV}^2,$$

where t is the square of invariant momentum transfer to the Be nucleus. The branching ratio, $[\phi(1020) \rightarrow K_L^0 K_S^0]/[\phi(1020) \rightarrow \text{all}]$, is taken to be 31%.[8] The decay angular distribution of the $\phi(1020)$ is required to be proportional to $\sin^2\beta$, where β is the angle between the direction of the K_L^0 in the $\phi(1020)$ rest system and the direction of the $\phi(1020)$ in the center-of-mass system.

The incoherent differential cross section is treated as an unknown to be determined in the present analysis. In terms of $p_\perp^2$ and the variable[37] $x = p_\parallel^*/p_{\max}^*$, where $p_\perp$ and $p_\parallel^*$ are the transverse and longitudinal momenta of the K_L^0 in the center-of-mass system and $p_{\max}^*$ is the kinematic maximum of the center-of-mass K_L^0 momentum, the differential cross section is

$$\left(\frac{d^2\sigma(k)}{dpd\cos\theta}\right)_{\text{incoherent}} = \frac{2p^2E^*}{Ep_{\max}^*}\frac{d^2\sigma(k)}{dxdp_\perp^2},$$

where E (E^*) is the energy of the K_L^0 in the laboratory (center-of-mass) system. In the notation of the invariant structure function,[37,38] we then have

$$\frac{E^*}{\pi p_{\max}^*}\frac{d^2\sigma(k)}{dxdp_\perp^2} = f(x, p_\perp^2, s),$$

where s is the square of the total energy in the center-of-mass system. The integrated structure function, $\mathcal{F}(x, s)$, is defined by

$$\mathcal{F}(x, s) \equiv \int_0^\infty dp_\perp^2 f(x, p_\perp^2, s).$$

If we assume that the hypotheses of scaling[37] and factorization[39,40] hold for all s and x, and if we parametrize the $p_\perp^2$ dependence as a single exponential, we then have

$$f(x, p_\perp^2, s) = \mathcal{F}(x)B\exp(-Bp_\perp^2),$$

a form which is approximately obeyed by the available data on $\pi^\pm$ and $K^\pm$ inclusive photoproduction from hydrogen.[41,42] For the exponential parameter we have used $B = 4.5\ (\text{GeV}/c)^{-2}$, a value consistent with the measurements of Boyarski *et al.*[42] With these approximations, the incoherent differential cross section becomes

$$\left(\frac{d^2\sigma}{dpd\cos\theta}\right)_{\text{incoherent}} = \left(\frac{2\pi p^2}{E}\right)B\exp(-Bp_\perp^2)\mathcal{F}(x).$$

The object of the analysis is then to find the magnitude and shape of $\mathcal{F}(x)$ which best reproduces the K_L^0 yield data. The procedure is possible since different values of the variable x contribute to distinctly different K_L^0 momenta, as is illustrated in Fig. 9. In this figure we show calculated K_L^0 yields as a function of p (for $\theta = 2°$, $E_0 = 16$ GeV, and $T = 1.75$ r.l.) corresponding to successive bins in $\mathcal{F}(x)$, where for the ith curve

$$\mathcal{F}(x) = 1\ \mu\text{b} \quad \text{for } x_i < x < x_{i+1}$$
$$= 0 \quad \text{for all other } x, \tag{3}$$

and where $x_i = \frac{1}{10}(i-1)$. Note that the observed yields receive contributions from $\mathcal{F}(x)$ only in the interval $0 \lesssim x \lesssim 1$.

The shape and magnitude of $\mathcal{F}(x)$ have been determined by a χ^2 minimization procedure as follows. First, the function $\mathcal{F}(x)$ is represented by a histogram for which the ith bin covers the region x_i to x_{i+1} and has a height given by the parameter α_i (μb). The incoherent yield for the jth data point (corresponding to $p = p_j$, $\theta = \theta_j$, $E_0 = E_{0j}$, and $T = T_j$)

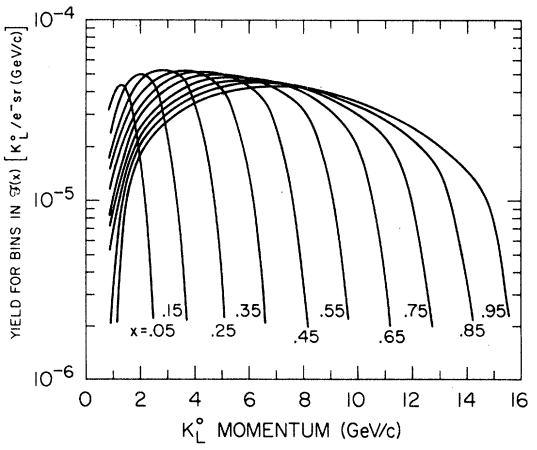

FIG. 9. Calculated yields for successive bins in $\mathcal{F}(x)$. The different curves result from distinct bins in $\mathcal{F}(x)$ which have widths of 0.1 in x and are centered at the indicated values of x (see text).

is then given by

$$Y_{\text{incoherent}}(j) = \sum_i \alpha_i y_{ij} ,$$

where the y_{ij} values are found by integrating Eq. (2) using $\mathfrak{F}(x)$ as in Eq. (3). Denoting the jth data point by D_j, χ^2 for the jth point is

$$\chi_j^2 = \left(\frac{D_j - S_j}{\Delta_j}\right)^2 ,$$

where

$$S_j = Y_{\text{coherent}}(j) + Y_{\text{incoherent}}(j) .$$

The denominator, Δ_j, is taken to be

$$\Delta_j = [(\delta D_j)^2 + (\epsilon D_j)^2]^{1/2} ,$$

where δD_j is the statistical uncertainty quoted in Tables IV and V, and $\epsilon = 0.10$ is our estimate of the systematic uncertainties expected between the various yield curves.

B. Discussion of Results

The results of the best fit are displayed in Figs. 5 and 6. The solid curves represent the sum of the coherent and incoherent yields, whereas the dashed curves represent the incoherent yields alone. The yield measurements for all energies, production angles, and target thicknesses are observed to be satisfactorily reproduced. As seen in Figs. 5 and 6, the major portion of yield arises from the incoherent contributions. The coherent

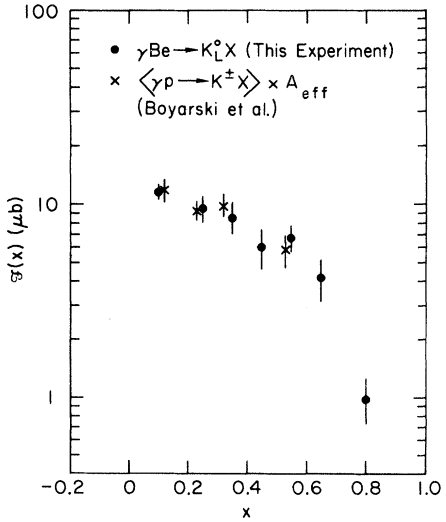

FIG. 10. Integrated structure function, $\mathfrak{F}(x)$, versus x. The solid circles are the values found in the present analysis for K_L^0 photoproduction from Be. For comparison, the average of K^+ and K^- data from hydrogen (Ref. 42) is also shown. The hydrogen data are multiplied by a factor $A_{\text{eff}} = 6$ in order to account for the Be target (see text).

TABLE VII. Integrated structure function for $\gamma\text{Be} \to K_L^0 X$.

x	$\mathfrak{F}(x)$ (μb)
0.0–0.2	11.4 ± 0.8
0.2–0.3	9.5 ± 1.6
0.3–0.4	8.6 ± 1.6
0.4–0.5	6.0 ± 1.4
0.5–0.6	6.7 ± 1.1
0.6–0.7	4.2 ± 0.9
0.7–0.9	1.0 ± 0.3

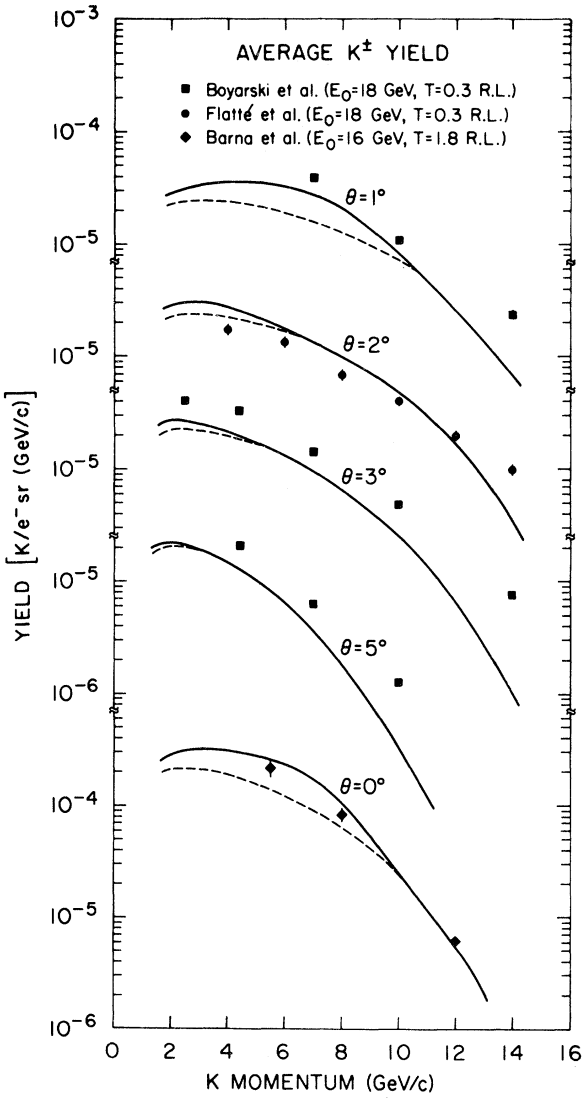

FIG. 11. Comparison of expected yields for K_L^0 from Be to the average of K^+ and K^- yields from Be. The data sources are (◆) Ref. 46, (●) Ref. 47, and (■) Ref. 48. The electron energies, production angles, and target thicknesses are indicated. The curves are calculated from the fitted values for $\mathfrak{F}(x)$ as explained in the text. The solid and dashed curves are as in the caption to Fig. 5.

$\phi(1020)$ contribution, which is ~15% of the total yield at 2°, is concentrated at low momenta and diminishes rapidly as the production angle is increased.

The fitted values for the integrated structure function, $\mathcal{F}(x)$, are given in Table VII and shown in Fig. 10. For the integral over x, we find $\int_0^1 dx\, \mathcal{F}(x) = 6.0\ \mu$b. The over-all systematic uncertainty in $\mathcal{F}(x)$ may be as large as 25%, arising from the over-all systematic uncertainties in the data, in the thick target approximation for the photon energy spectrum, and in the theoretical assumptions of scaling and factorization.

It is interesting to compare the values of $\mathcal{F}(x)$ for Be to those for hydrogen. In Fig. 10 we also show the preliminary data of Boyarski *et al.*[42] for the average of K^+ and K^- inclusive photoproduction from hydrogen at 18 GeV.[43] The charged-K results agree well in shape with the K_L^0 results, differing only by a scale factor, A_{eff}. A_{eff} can be interpreted as the effective number of nucleons contributing to the incoherent particle production. For the present comparison we find $A_{\text{eff}} = 6$, in agreement with the empirical relation, $A_{\text{eff}} = A^{0.9}$, which applies over a wide range of photon energies in the measurement of γA total cross sections.[44,45] Thus the inclusive photoproduction of particles from light nuclei and from hydrogen appear to be related simply by the factor A_{eff}. For nuclei much heavier than Be, the relation $A_{\text{eff}} = A^{0.9}$ is likely to be modified because of the opposing effects of (a) nuclear absorption of the photoproduced kaons and (b) production of kaons in multistep processes such as $\gamma N \to \pi X$, $\pi N \to KX'$.

As a further test of the present analysis, we compare in Fig. 11 the average of K^+ and K^- photoproduction yields from electrons on Be targets[46-48] to the expected K_L^0 yields.[49] Generally reasonable agreement is found, although there are large systematic differences between the experiments.

Extrapolations of K_L^0 yields to higher energies for several different Be target thicknesses have also been made. The yields for 2° production from a 1.0-r.l. Be target at energies of 30, 40, and 50 GeV are given in Fig. 12. The yields for 2° production from 0.5-, 1.0-, and 2.0-r.l. Be targets at an energy of 40 GeV are given in Fig. 13.

In conclusion, the interpretation presented in this paper successfully describes the K_L^0 photoproduction yields, together with the average of K^+ and K^- photoproduction yields, over a wide range of electron energies, production angles, and target thicknesses. In addition, we find that the inclusive photoproduction of particles from light nuclei and from hydrogen appear to be related simply by a multiplicative factor, A_{eff}, the effective number of nucleons in the target nucleus. The success of the inclusive interpretation allows us with confidence to extrapolate K_L^0 yields to 50 GeV.

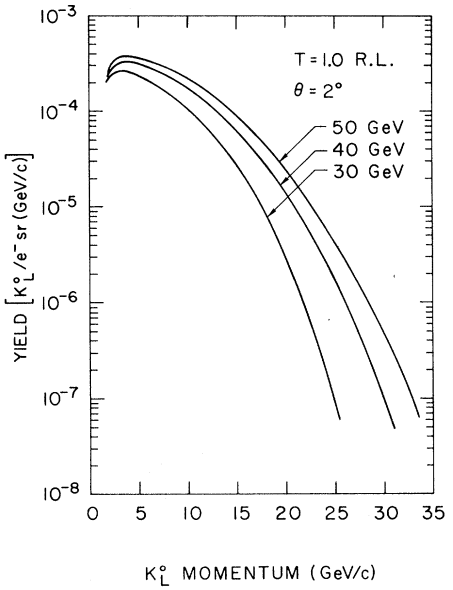

FIG. 12. Predicted yields of K_L^0 mesons for 2° production from a 1.0-r.l. Be target at electron energies of 30, 40, and 50 GeV.

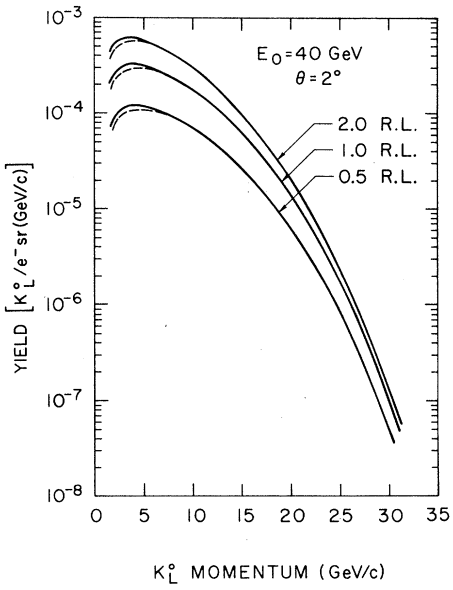

FIG. 13. Predicted yields of K_L^0 mesons for 2° production from 0.5-, 1.0-, and 2.0-r.l. Be targets at an electron energy of 40 GeV.

ACKNOWLEDGMENTS

We wish to thank A. Kilert, W. Walsh, A. Baumgarten, and R. Vetterlein for help in design and construction of the neutral beam. We are grateful for the assistance given to us by R. Watt and the crew of the SLAC 40-in. bubble chamber, by J. Brown and the film analysis group at SLAC, and by D. Johnson.

*Work supported in part by the U. S. Atomic Energy Commission.

†Now at Duke University, Durham, North Carolina.

‡Now at the University of Toronto, Toronto, Canada.

§Now at the University of Washington, Seattle, Washington.

‖Now at the University of California (Riverside), Riverside, California.

**Now at the National Accelerator Laboratory, Batavia, Illinois.

[1]A. D. Brody, W. B. Johnson, D. W. G. S. Leith, G. Loew, J. S. Loos, G. Luste, R. Miller, K. Moriyasu, B. C. Shen, W. M. Smart, and R. Yamartino, Phys. Rev. Letters 22, 966 (1969).

[2]D. G. Cassel, E. Engels, Jr., A. C. Entis, and A. Sadoff, Phys. Letters 34B, 223 (1971).

[3]M. G. Albrow, D. Aston, D. P. Barber, L. Bird, R. J. Ellison, C. Halliwell, A. E. Harckham, F. K. Loebinger, P. G. Murphy, J. Walters, A. J. Wynroe, and R. F. Templeman, Nucl. Phys. B23, 509 (1970).

[4]J. F. Shivell, E. Engels, Jr., A. Entis, J. M. Paterson, L. N. Hand, and A. Sadoff, Phys. Rev. Letters 19, 1349 (1967).

[5]C. D. Buchanan, C. Y. Chien, B. Cox, E. Dally, D. F. Drickey, L. Ettlinger, P. Innocenti, F. D. Rudnick, E. Seppi, P. F. Shepard, D. H. Stork, H. K. Ticho, R. A. Zdanis, D. Berk, A. Grigorian, and L. Resvanis, Phys. Letters 32B, 396 (1970).

[6]R. S. Larsen and D. Horelick, SLAC Report No. SLAC-PUB-398, 1968 (unpublished).

[7]A small fraction of true K_{e3} decays failed to have a kinematic solution due to measurement resolution or small-angle scatters on the electron track. Events in this category are readily identifiable and have been included in the analysis of the K_L^0 spectrum. Only 7% of the total sample are in this category.

[8]The lifetime and decay properties of K_L^0 and $\phi(1020)$ mesons are taken from the compilation of the Particle Data Group, Phys. Letters 39B, 1 (1972).

[9]The Monte Carlo calculations have been done using the values $\xi(0) = -0.85$, $\lambda_+ = 0.045$ (parameters for the leptonic decay), and $A = -0.25$ (parameter for the $\pi^+\pi^-\pi^0$ decay). However, the K_L^0 momentum spectrum determined in the present analysis is insensitive to the choice of matrix element parameters. A sample analysis using simple phase space for the Monte Carlo events produced a K_L^0 momentum spectrum well within the statistical uncertainties.

[10]In order to ensure a smooth behavior of the α_j^* versus p_K, a contribution is added to χ^2 which for the jth bin is proportional to

$$\left[\left(\frac{\alpha_{j+1}-\alpha_j}{\Delta p_{Kj}}\right)-\left(\frac{\alpha_j-\alpha_{j-1}}{\Delta p_{Kj-1}}\right)\right]^2.$$

This additional term forces a smooth behavior of $dZ(p_K)/dp_K$ without significantly changing the original χ^2 value.

[11]A. Böhm, P. Darriulat, C. Grosso, V. Kaftanov, K. Kleinknecht, H. L. Lynch, C. Rubbia, H. Ticho, and K. Tittel, Nucl. Phys. B9, 605 (1969).

[12]W. L. Lakin, E. B. Hughes, L. H. O'Neill, J. N. Otis, and L. Madansky, Phys. Letters 31B, 677 (1970).

[13]R. J. Abrams, R. L. Cool, G. Giacomelli, T. F. Kycia, B. A. Leontic, K. K. Li, A. Lundby, D. N. Michael, and J. Teiger, Phys. Rev. D 4, 3235 (1971).

[14]The K_L^0-Pb absorption cross sections have been measured by comparing the K_L^0 flux at the chamber with and without an additional 130 g/cm^2 Pb in the neutral beam.

[15]Expressing p_K in GeV/c and σ in mb, the parameters for the best fits to the cross section are $b_1 = 14.76$, $b_2 = 0.00423$, $b_3 = 19.21$, $n_1 = 0.754$, $n_2 = 0.874$, $b_4 = 7.63$, $b_5 = 17.50$, and $n_3 = 0.804$.

[16]R. L. Cool, G. Giacomelli, T. F. Kycia, B. A. Leontic, K. K. Li, A. Lundby, J. Teiger, and C. Wilkin, Phys. Rev. D 1, 1887 (1970).

[17]R. J. Abrams, R. L. Cool, G. Giacomelli, T. F. Kycia, B. A. Leontic, K. K. Li, and D. N. Michael, Phys. Rev. D 1, 1917 (1970).

[18]W. Galbraith, E. W. Jenkins, T. F. Kycia, B. A. Leontic, R. H. Phillips, A. L. Read, and R. Rubinstein, Phys. Rev. 138, B913 (1965).

[19]A. P. Batson, B. B. Culwick, H. B. Klepp, and L. Riddiford, Proc. Roy. Soc. (London) A251, 233 (1959).

[20]H. O. Cohn, R. D. McCulloch, W. M. Bugg, and G. T. Condo, Nucl. Phys. B21, 505 (1970).

[21]D. C. Brunt, M. J. Clayton, and B. A. Westwood, Phys. Rev. 187, 1856 (1969).

[22]A. Shapira, O. Benary, Y. Eisenberg, E. E. Ronat, D. Yaffe, and G. Yekutieli, Phys. Rev. Letters 21, 1835 (1968).

[23]J. G. Rushbrooke, D. V. Bugg, A. J. Oxley, J. A. Zoll, M. Jobes, J. Kinson, L. Riddiford, and B. Tallini, Nuovo Cimento 33, 1509 (1964).

[24]A. Gasparyan, A. V. Nikitin, and Yu. A. Troyan, Yad. Fiz. 14, 764 (1971) [Sov. J. Nucl. Phys. 14, 429 (1972)].

[25]W. Shimmerling, T. J. Devlin, W. W. Johnson, K. G. Vosburgh, and R. E. Mischke, Phys. Rev. C 7, 248 (1973).

[26]N. E. Booth, G. W. Hutchinson, and B. Ledley, Proc. Phys. Soc. (London) 71, 293 (1958).

[27]T. Coor, D. A. Hill, W. F. Hornyak, L. W. Smith, and G. Snow, Phys. Rev. 98, 1369 (1955).

[28]V. P. Dzhelepov, V. I. Satarov, and B. M. Golovin, Zh. Eksp. Teor. Fiz. 29, 369 (1955) [Sov. Phys. JETP 2, 349 (1959)].

[29]E. F. Parker, T. Dobrowolski, H. R. Gustafson, L. W. Jones, M. J. Longo, F. E. Ringia, and B. Cork, Phys. Letters 31B, 250 (1970).

[30]J. Engler, K. Horn, F. Mönnig, P. Schludecker, W. Schmidt-Parzefall, H. Schopper, P. Sievers, H. Ulrich, R. Hartung, K. Runge, and Yu. Galaktionov, Phys. Letters 32B, 716 (1970).

[31]R. E. Mischke, T. J. Devlin, W. Johnson, J. Norem, K. Vosburgh, and W. Schimmerling, Phys. Rev. Letters 25, 1724 (1970).

[32]E. F. Parker, T. Dobrowolski, H. R. Gustafson, L. W. Jones, M. J. Longo, F. E. Ringia, and B. Cork, Phys. Letters 31B, 246 (1970).

[33]J. Engler, K. Horn, J. König, F. Mönnig, P. Schludecker, H. Schopper, P. Sievers, H. Ulrich, and K. Runge, Phys. Letters 28B, 64 (1968).

[34]The analagous production of particles by virtual photons (electroproduction) also occurs. However, for the present application we can ignore the electroproduction of particles since the ratio of the contribution of virtual/real photons is approximately $0.02/T$, where T is the target thickness in units of radiation lengths. For a further discussion, see L. Hand and R. Wilson, SLAC Report No. 25, 1963 (unpublished), Part II.

[35]Y. S. Tsai and Van Whitis, Phys. Rev. 149, 1248 (1966).

[36]G. McClellan, N. Mistry, P. Mostek, H. Ogren, A. Osborne, J. Swartz, R. Talman, and G. Diambrini-Palazzi, Phys. Rev. Letters 26, 1593 (1971).

[37]R. P. Feynman, Phys. Rev. Letters 23, 1415 (1969).

[38]For a review of inclusive reactions, see for example, W. R. Frazer, L. Ingber, C. H. Mehta, C. H. Poon, D. Silverman, K. Stowe, P. D. Ting, and H. J. Yesian, Rev. Mod. Phys. 44, 284 (1972).

[39]N. F. Bali, L. S. Brown, R. D. Peccei, and A. Pignotti, Phys. Rev. Letters 25, 557 (1970).

[40]J. L. Day, N. P. Johnson, A. D. Krisch, M. L. Marshak, J. K. Randolph, P. Schmueser, G. J. Marmer, and L. G. Ratner, Phys. Rev. Letters 23, 1055 (1969).

[41]K. C. Moffeit, J. Ballam, G. B. Chadwick, M. Della-Negra, R. Gearhart, J. J. Murray, P. Seyboth, C. K. Sinclair, I. O. Skillicorn, H. Spitzer, G. Wolf, H. H. Bingham, W. B. Fretter, W. J. Podolsky, M. S. Rabin, A. H. Rosenfeld, R. Windmolders, G. P. Yost, and R. H. Milburn, Phys. Rev. D 5, 1603 (1972).

[42]A. M. Boyarski, D. Coward, S. Ecklund, B. Richter, D. Sherden, R. Siemann, and C. Sinclair, in *Proceedings of the International Symposium on Electron and Photon Interactions at High Energies, 1971,* edited by N. B. Mistry (Cornell Univ. Press, Ithaca, N. Y., 1972); D. Sherden, private communication.

[43]Values for $\mathcal{F}(x)$ for hydrogen have been evaluated from the data in Ref. 42 by assuming $Ed^3\sigma/dp^3 = B \times \exp(-Bp_\perp^2)\mathcal{F}(x)$, and using $B = 4.4$ GeV^{-2}. In making the comparison of K_L^0 photoproduction from Be with $K^\pm$ photoproduction from hydrogen, we ignore possible systematic differences due to isospin and regeneration.

[44]D. O. Caldwell, V. B. Elings, W. P. Hesse, G. E. Jahn, R. J. Morrison, F. V. Murphy, and D. E. Yount, Phys. Rev. Letters 23, 1256 (1969).

[45]V. Heynen, H. Meyer, B. Naroska, and D. Notz, Phys. Letters 34B, 651 (1971).

[46]A. Barna, J. Cox, F. Martin, M. L. Perl, T. H. Tan, W. T. Toner, T. F. Zipf, and E. H. Bellamy, Phys. Rev. Letters 18, 360 (1967).

[47]S. M. Flatté, J. J. Murray, P. R. Klein, L. H. Johnston, and S. G. Wojcicki, Phys. Rev. 166, 1482 (1968).

[48]A. M. Boyarski, F. Bulos, W. Busza, R. Diebold, S. D. Ecklund, G. E. Fischer, J. R. Rees, and B. Richter, SLAC Users Handbook, 1971 (unpublished), Sec. C.2.

[49]The calculated curves are identical to the expected K_L^0 yields except that the branching ratio of $\phi(1020)$ into charged kaons has been used (see Ref. 8).